NJC

ROYAL SOCIETY OF CHEMISTRY

PAPER

View Article Online
View Journal | View Issue

Cite this: *New J. Chem.*, 2024, **48**, 10830

Photoluminescence properties of europium-activated double layered perovskite $Sr_3Ti_2O_7$ for high-quality lighting applications†

Dhananjay Kumar Singh, *[ab] Shriya Sinha [ac] and Manoj Kumar Mahata *[d]

We present a comprehensive investigation into the concentration and temperature-dependent photoluminescence (PL) properties of europium ion (Eu^{3+}) activated double-layered perovskite $Sr_3Ti_2O_7$ materials. We conducted thorough analyses to assess their phase purity, crystal structure, surface morphology, and optical properties to gain a complete understanding. The double-layered perovskite $Sr_3Ti_2O_7$:Eu^{3+} exhibited a tetragonal phase with space group *I*4/*mmm*. When excited by 395 nm ultraviolet (UV) light, the prepared materials exhibited a firm red emission peak at 616 nm, indicating the hypersensitive electric dipole transition $^5D_0 \rightarrow {}^7F_2$ in Eu^{3+} ions. The quantum yield of the optimized sample was estimated to be 18%. To explore the temperature-dependent behavior of the photoluminescence, measurements were carried out over a wide range of temperatures from 300 K to 450 K. Notably, the phosphors demonstrated significant thermal stability, with 75% of the emission intensity retained at 420 K compared to 300 K. These findings signify the material's ability to maintain its luminescent properties at elevated temperatures. The photometric characterization of $Sr_3Ti_2O_7$:Eu^{3+} further validated its red emission capability. Moreover, we employed the Judd–Ofelt approach to examine the radiative intensity parameters (Ω_2, Ω_4, Ω_6). The obtained results provide substantial support for the promising prospects of this perovskite material in the rapidly growing field of solid-state lighting and display devices.

Received 1st February 2024,
Accepted 12th May 2024

DOI: 10.1039/d4nj00551a

rsc.li/njc

Introduction

In recent decades, the scientific community has been confronted with concerns about meeting energy demands. As a result, researchers have been incessantly exploring luminescent materials in search of novel technologies that can address these challenges, particularly in display technology and lighting systems.[1–3] Notably, there has been a surge of interest in white light-emitting diodes (W-LEDs) as a potential next-generation solid-state lighting solution, surpassing the traditional fluorescent and incandescent lamps. This interest stems from the superior attributes of W-LEDs, including enhanced energy efficiency, environmental compatibility, high luminous efficiency, compact form factor, rapid response time, and extended operational lifespan.[4,5] Thus far, the realization of W-LEDs has commonly relied on the integration of a blue-emitting gallium nitride (GaN) light-emitting diode in combination with yellow light-emitting materials such as yttrium aluminum garnet doped with cerium ions $Y_3Al_5O_{12}$:Ce^{3+}.[6] However, the resulting devices exhibit a highly correlated color temperature (CCT) and a low color rendering index (CRI < 80) due to the inadequate contribution of red light, thereby limiting their applicability in certain contexts.[7,8] Consequently, it becomes imperative to address this issue by developing highly luminescent red phosphors possessing exceptional spectral characteristics that can be efficiently activated in the near-UV range. The enhancement of red-emitting materials has emerged as a prominent area of research within lighting applications, particularly for applications necessitating high-quality color rendering and full-color displays.

Among the array of red-emitting species, the Eu^{3+} ion has garnered significant attention as an excellent doping candidate for W-LEDs. The Eu^{3+} ion possesses an electronic configuration of $[Xe]4f^6$, wherein the 4f orbitals are effectively shielded from external influences by the closed outer shells of $5s^2$ and $5p^6$. Notably, the ground state energy level $^7F_0$ and the highly significant excited state energy level $^5D_0$ of Eu^{3+} are nondegenerate and remain unaffected by the crystal-field effect exerted by the host material. This important characteristic simplifies the interpretation of experimental absorption and luminescence spectra associated with Eu^{3+}. Consequently, Eu^{3+} ions have gained recognition as efficient activators, exhibiting narrow emission profiles and superior optical

[a] *Department of Physics, Indian Institute of Technology (Indian School of Mines), Dhanbad-826004, India. E-mail: drdksingh.physics@gmail.com*
[b] *Department of Physics, Government Polytechnic Siwan, Bihar – 841203, India*
[c] *Department of Physics, Shahid Chandrashekhar Azad Govt. P. G. College, Jhabua, Madhya Pradesh – 457661, India*
[d] *Third Institute of Physics, Georg-August-Universität Göttingen, Friedrich-Hund-Platz 1, Göttingen-37077, Germany. E-mail: mmahata@phys.uni-goettingen.de*

† Electronic supplementary information (ESI) available. See DOI: https://doi.org/10.1039/d4nj00551a

properties due to f–f and f–d transitions. Numerous reports have demonstrated the intense photoluminescence behavior of Eu^{3+} ions in various host materials, primarily attributed to the $^5D_0 \rightarrow {}^7F_j$ (j = 0–6). Remarkably, when Eu^{3+} ions occupy non-centrosymmetric sites, they emit vibrant red light corresponding to the $^5D_0 \rightarrow {}^7F_2$ transitions.[9,10] It is well-established that the optical properties of luminescent materials doped with rare earth ions are profoundly influenced by the characteristics of the host matrix.[11] The majority of previous research has focused on the optical properties of rare-earth ion-activated perovskite $ATiO_3$ (A = Ca, Sr, Ba) hosts,[11–16] with various applications.[17,18] To achieve superior optical properties, it is crucial for the host material, in addition to an appropriate activator, to exhibit chemical and physical stability and low phonon energy. Low-phonon host materials are highly appreciated for enhancing luminescence efficiency by minimizing non-radiative decay losses. These losses, where energy is dissipated as heat rather than light emission, are significantly reduced in materials with low-phonon energy. Consequently, such materials exhibit a higher probability of radiative transitions and longer excited-state lifetimes, resulting in enhanced luminescence efficiency and higher quantum yields. Therefore, host materials with low lattice vibrational energy enable more efficient energy conversion into luminescence. The specific arrangement of Sr and Ti layers in $Sr_3Ti_2O_7$ influences phonon modes, contributing to an overall lower phonon energy ($\sim$760 cm^{-1}) compared to other materials.[19] Thus, $Sr_3Ti_2O_7$ is an ideal host material for rare-earth ions, facilitating efficient energy transfer processes and supporting the desired optoelectronic properties.

Structurally, $Sr_3Ti_2O_7$ is closely related to the cubic phase $SrTiO_3$ and represents one of the intergrowth phases, known as Ruddlesden–Popper-RP phases, derived from $SrTiO_3$ with a general formula $Sr_2(Sr_{n-1}Ti_nO_{3n+1})$ where n = 2.[18,20] Above all, layered perovskite compounds offer the advantage of accommodating higher doping concentrations of rare-earth ions due to the increased distance between layers. Consequently, these compounds serve as excellent host materials for dopants. Zhang *et al.* initially studied this material and focussed on the charge compensation mechanism and its effect on the luminescence property with the introduction of K^+ ions in the lattice of $Sr_3Ti_2O_7$:Eu^{3+}.[21] In the case of $Sr_3Ti_2O_7$, the material exhibits a tetragonal structure with a specific layer arrangement, comprising three layers of SrO followed by two layers of TiO_2. This distinctive structure results in an increased distance between layers compared to $SrTiO_3$. On the other hand, $SrTiO_3$ consists of a more straightforward, single-layer structure with alternating SrO and TiO_2 layers.[22,23]

Thus, this study aims to comprehensively investigate the structural, optical, and spectroscopic properties of layered perovskite $Sr_3Ti_2O_7$: Eu^{3+}. The ultimate objective of this research is to explore the potential of layered perovskite $Sr_3Ti_2O_7$: Eu^{3+} for use in W-LEDs, particularly as a suitable candidate for near-UV LED chips.

Experimental

All the samples were synthesized using the conventional solid-state reaction method, employing stoichiometric relationships of $Sr_{3(1-x)}Ti_2O_7$:xEu^{3+} (x = 0, 1, 2, 3, 5, 7 mol%). The starting precursors, namely $SrCO_3$ (99%, Merck), TiO_2 (99%, Merck) and Eu_2O_3 (99.9% Otto) were of standard grade and were used without further purification. To ensure homogeneity, the chemicals were ground in the presence of ethanol for 2 h using an agate mortar. Subsequently, the mixture was annealed at 1300 °C for 3 h within a programmable electric furnace. Finally, the resulting materials were naturally cooled to room temperature and ground into a fine powder form to facilitate further structural and optical characterizations.

The crystalline phases of the prepared perovskite $Sr_{3(1-x)}Ti_2O_7$:xEu^{3+} were determined using a powder X-ray diffractometer (D8 advanced, Brucker) equipped with a Cu tube with K_α radiation (λ = 0.15406 nm), with scanning conducted in the 20°–80° 2θ range. The surface characteristics of the fabricated materials were investigated by using a field emission scanning electron microscope (FESEM), employing the 55-Supra instrument from Germany. Photoluminescence measurements, including decay kinetics, were performed using the Agilent Technologies Cary Eclipse Fluorescence Spectrophotometer. The temperature-dependent photoluminescence spectra were also recorded using the same spectrophotometer equipped with an Optistate DN2 (Oxford Cryostat) for precise temperature control. The quantum yield of the optimized phosphor was determined using the Horiba Acton 2500 Spectrophotometer, with excitation provided by a xenon arc lamp.

Results and discussion

Structural studies: phase purity and morphological analysis

In the present study, investigation of the phase purity and crystal structure of $Sr_{3(1-x)}Ti_2O_7$:xEu^{3+} phosphors was carried out using X-ray diffraction (XRD) analysis. As depicted in Fig. 1(a), the obtained results revealed that the diffraction peaks observed in the prepared samples perfectly matched the Joint Committee on Powder Diffraction Standards (JCPDS) card no. 78-2479. This correspondence indicates that the crystal structure of $Sr_3Ti_2O_7$ belongs to the space group $I4/mmm$, characterized by tetragonal symmetry. Within the unit cell of $Sr_3Ti_2O_7$, two cubic perovskite ($SrTiO_3$) layers are separated by a single SrO layer.[18] It is worth mentioning that certain Sr ions occupy positions between the perovskite layers, which are 9 oxygen-ion coordinated sites with C_{4v} symmetry. The distances between the strontium and oxygen atoms, denoted as d (Sr–O) values, were measured to be 0.249 nm, 0.265 nm, and 0.277 nm.[20]

Additionally, other Sr occupy positions at the center of the perovskite layer, which are 12 oxygen-ion coordinated sites with D_{4h} symmetry. The corresponding d (Sr–O) values for these positions were 0.2760 nm and 0.2764 nm.[20] The XRD analysis revealed that the prominent peaks observed at 2θ = 31.72° and 32.41° could be indexed to the Miller indices (105) and (110), respectively. These peaks are particularly noteworthy among the others detected in the diffraction pattern. Notably, the results indicated that introducing Eu^{3+} dopants did not significantly alter the crystallinity of $Sr_3Ti_2O_7$. Moreover, the XRD

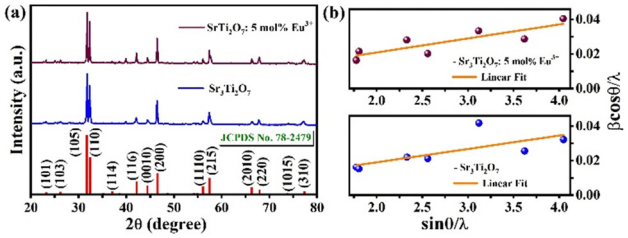

Fig. 1 (a) X-ray diffraction pattern of undoped $Sr_3Ti_2O_7$ and 5 mol% Eu^{3+} doped $Sr_3Ti_2O_7$ with standard JCPDS data. (b) Williamson–Hall plots of undoped $Sr_3Ti_2O_7$ and 5 mol% Eu^{3+} doped $Sr_3Ti_2O_7$.

patterns displayed no indications of any additional phases or impurities present in the samples. This observation suggests that the Eu^{3+} ions were uniformly dispersed throughout the host lattice. The ionic radii of Eu^{3+} and Sr^{2+} ions are 1.12 Å and 1.31 Å, respectively, with a coordination number of 9. The ionic radius of the Eu^{3+} ion is smaller than the ionic radius of Sr^{2+} ions. So, it would be successfully incorporated into the $Sr_3Ti_2O_7$ matrix. Thus, we can infer that the Eu^{3+} ions would occupy the sites of Sr^{2+} ions in the $Sr_3Ti_2O_7$ host lattices.[21,24] Moreover, a shift toward higher angles in the diffraction peaks was observed due to substituting Sr^{2+} ions by smaller Eu^{3+} ions.

The average crystallite size of undoped $Sr_3Ti_2O_7$ and 5 mol% Eu^{3+} doped $Sr_3Ti_2O_7$ was performed utilizing two established equations: the Debye–Scherrer formula and Williamson–Hall (W–H) equation.[25,26]

The Debye–Scherrer formula, which is widely employed for calculating crystallite size in XRD patterns, and the Williamson–Hall equation, which incorporates additional parameters to account for strain broadening effects, are given by:

$$D = \frac{0.89\lambda}{\beta\cos\theta} \text{ and } \frac{\beta\cos\theta}{\lambda} = \frac{1}{D} + \frac{\varepsilon\sin\theta}{\lambda} \quad (1)$$

Here, D represents the mean crystallite size, β denotes the full-width half-maxima (FWHM), λ stands for the wavelength of incident X-ray radiation, θ represents the Bragg's angle of diffraction, and ε signifies the micro-strain.

Fig. 1(b) presents the Williamson–Hall plots for $Sr_{3(1-x)}Ti_2O_7$:xEu^{3+} phosphors, which offer valuable insights into the structural parameters. The crystallite size and micro-strain values were calculated using the Debye–Scherrer and Williamson–Hall equations, respectively. A summary of these parameters can be found in Table 1.

It is worth noting that there is a slight difference in the crystallite size between the undoped $Sr_3Ti_2O_7$ and 5 mol% Eu^{3+} doped $Sr_3Ti_2O_7$. This disparity can be attributed to the mismatch in ionic radii between the Eu^{3+} and Sr^{2+} ions. Introducing Eu^{3+} ions into the crystal lattice may cause subtle alterations in the crystallite size due to this mismatch.

The surface morphology and microstructure analysis of the undoped $Sr_3Ti_2O_7$ and 5 mol% Eu^{3+} doped $Sr_3Ti_2O_7$ materials were characterized using FESEM. The obtained results are presented in Fig. 2(a and b).

Table 1 Structural parameters for Eu^{3+} doped $Sr_3Ti_2O_7$

	Crystallite size		
Concentration (mol %)	Debye–Scherrer (nm)	Williamson–Hall (nm)	Micro-strain (10^{-3})
Eu^{3+} 0 mol %	22–55	22	7.78
Eu^{3+} 5 mol %	21–58	29	8.16

In the case of the undoped $Sr_3Ti_2O_7$ sample, it was observed that the particles exhibited an irregular and agglomerated spherical shape. The average size of these particles was determined to be approximately 180 nm. However, the morphology showed minimal changes upon introducing 5 mol% Eu^{3+} dopants into the $Sr_3Ti_2O_7$ lattice. The particle size slightly increased to an average of 225 nm. This variation in particle size can be attributed to the uncontrolled heat flow during the annealing process of the samples. The 5 mol% Eu^{3+} doped $Sr_3Ti_2O_7$ had a larger particle size than the undoped $Sr_3Ti_2O_7$. A histogram was presented to visualize particle distribution, as depicted in Fig. 2(c and d). This representation provides a clear understanding of the particle distribution within the samples.

Overall, the FESEM analysis revealed the surface morphology and particle characteristics of the undoped $Sr_3Ti_2O_7$ and 5 mol% Eu^{3+} doped $Sr_3Ti_2O_7$, highlighting the impact of Eu^{3+} doping on the particle size and morphology.

Optical properties and Judd–Ofelt analysis

Steady-state photoluminescence. In studying Eu^{3+}-activated $Sr_3Ti_2O_7$ materials, extensive spectroscopic investigations were conducted to examine their PL excitation, emission spectra, and decay kinetics. The PL excitation spectra, as depicted in the inset of Fig. 3(a), were recorded within the 225–500 nm range.

The excitation spectra of the prepared phosphors were observed while monitoring the emission at 616 nm, corresponding to the $^5D_0 \rightarrow {}^7F_2$ transition. The excitation spectra

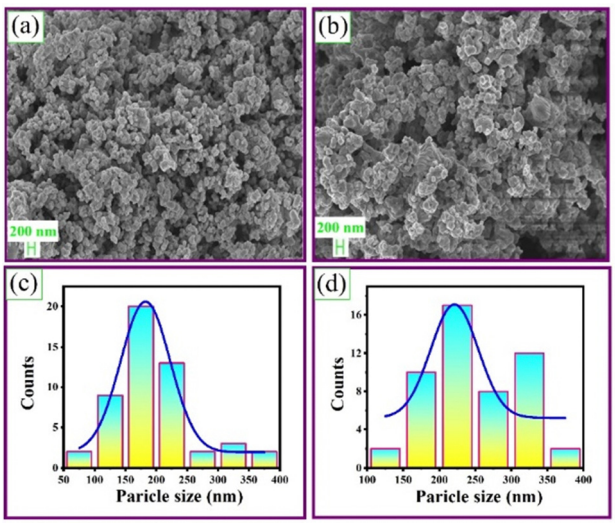

Fig. 2 FESEM image of (a) undoped $Sr_3Ti_2O_7$ and (b) 5 mol% Eu^{3+} doped $Sr_3Ti_2O_7$; (c) and (d) histogram plot of particles distribution of undoped $Sr_3Ti_2O_7$ and 5 mol% Eu^{3+} doped $Sr_3Ti_2O_7$.

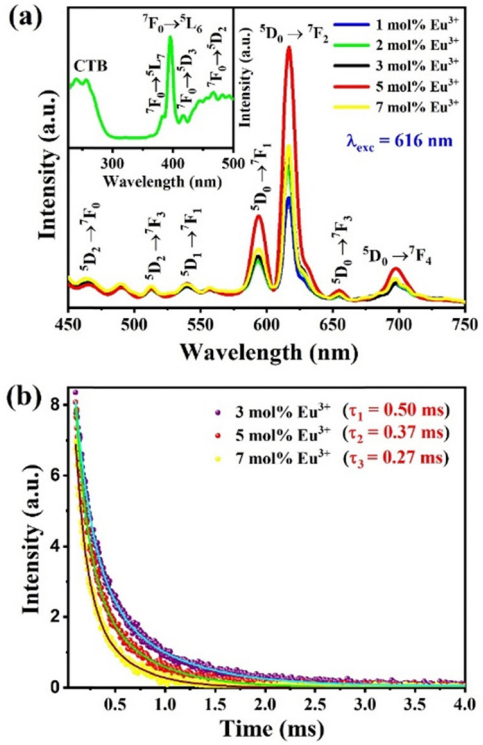

Fig. 3 (a) Variation of the PL emission spectra of $Sr_3Ti_2O_7$:xEu^{3+} at various concentrations of Eu^{3+}. The inset shows the PL excitation spectra of 5 mol% doped $Sr_3Ti_2O_7$. (b) PL decay time profile at three different concentrations of Eu^{3+}.

exhibited two distinct regions, with the first region corresponding to the charge transfer band (CTB) between the host material and Eu^{3+} ions, observed at lower wavelengths. In contrast, the second region represented the f–f transitions within the Eu^{3+} ions, which were visible in the higher wavelength region of the spectrum.

Specifically, the charge transfer band ($O^2 \rightarrow Eu^{3+}$) appeared at 250 nm, indicating a sufficient covalency between the oxygen 2p orbitals (O^{2-}) and the partially filled f orbital of the Eu^{3+} ion.

Moreover, the excitation spectra displayed several sharp peaks in the higher wavelength region, attributed to the characteristic f–f transitions of Eu^{3+} ions.[27] These peaks originated from transitions between the ground state $^7F_0$ and various excited states of the Eu^{3+} ion upon absorption of UV light. These transitions were centered at 382 nm ($^7F_0 \rightarrow {}^5L_7$), 395 nm ($^7F_0 \rightarrow {}^5L_6$), 415 nm ($^7F_0 \rightarrow {}^5D_3$), and 464 nm ($^7F_0 \rightarrow {}^5D_2$).[28] Among these sharp and intense peaks, the most prominent one was centered at 395 nm, corresponding to the transition $^7F_0 \rightarrow {}^5L_6$. This observation suggests that the $^5L_6$ level is highly populated when excited with UV light at 395 nm. Additionally, the excitation spectra of the layered perovskite $Sr_3Ti_2O_7$:Eu^{3+} aligned well with near UV LEDs and blue chips, indicating that a 395 nm excitation wavelength is suitable for monitoring the photoluminescence emission spectra of Eu^{3+} activated $Sr_3Ti_2O_7$.

Fig. 3(a) depicts the photoluminescence emission spectra of $Sr_{3(1-x)}Ti_2O_7$:xEu^{3+} for various concentrations of Eu^{3+} ions. The emission spectra were obtained by monitoring the most intense excitation transition $^7F_0 \rightarrow {}^5L_6$ at 395 nm and recorded in the 450 to 750 nm range. The spectra exhibit a characteristic emission profile attributed to the Eu^{3+} ions, which consists of $^5D_0 \rightarrow {}^7F_J$ (J = 1, 2, 3, 4) transitions. Among these transitions, the most prominent peak corresponds to the $^5D_0 \rightarrow {}^7F_2$ transition at 616 nm. Additionally, several other peaks located at 470, 520, 540, 559, 596, 654, and 701 nm can be assigned to optical transitions $^5D_2 \rightarrow {}^7F_0$, $^5D_2 \rightarrow {}^7F_3$, $^5D_1 \rightarrow {}^7F_1$, $^5D_1 \rightarrow {}^7F_2$, $^5D_0 \rightarrow {}^7F_1$, $^5D_0 \rightarrow {}^7F_3$ and $^5D_0 \rightarrow {}^7F_4$, respectively.[29] The 596 nm transition from $^5D_1 \rightarrow {}^7F_1$ is known as a magnetic dipole transition, while the 616 nm transition from $^5D_0 \rightarrow {}^7F_2$ is attributed to the forced electric dipole transition. These transitions are sensitive to the crystal field's symmetry and the local environment.[25] The transition from $^5D_0 \rightarrow {}^7F_2$ is categorized as a "hypersensitive transition", adhering to the selection rules $|S| = 0$, $|L| \leq 2$, and $|J| \leq 2$. Its intensity is significantly influenced by the local symmetry of the Eu^{3+} ion and the nature of the ligands compared to other electric dipole transitions.[30]

When the Eu^{3+} ions occupy a site with low symmetry, the red emission from the $^5D_0 \rightarrow {}^7F_2$ transition is dominant. On the contrary, if the ions are situated at a site with inversion symmetry, the magnetic dipole transition, denoted as $^5D_0 \rightarrow {}^7F_1$, assumes a more prominent and influential role. The asymmetry ratio, as shown in Table 2, which measures the ratio of the integrated area of the electric dipole transition $^5D_0 \rightarrow {}^7F_2$ to the magnetic dipole transition $^5D_0 \rightarrow {}^7F_1$, indicates that the Eu^{3+} ion is situated at a site without inversion symmetry, as the ratio is greater than 1. On the other hand, if the magnetic dipole transition $^5D_0 \rightarrow {}^7F_1$ dominates over the electric dipole transition $^5D_0 \rightarrow {}^7F_2$, it suggests that the Eu^{3+} ion is located at a site with inversion symmetry.[28,30] Fig. 3(a) reveals that as the concentration of Eu^{3+} ions increases in the layered $Sr_3Ti_2O_7$ host, the intensity of the $^5D_0 \rightarrow {}^7F_2$ transition initially increases, reaching its maximum value at 5 mol% of Eu^{3+} and subsequently decreasing. This decrease in emission intensity is attributed to the phenomenon of concentration quenching. Concentration quenching is observed at higher doping concentrations of Eu^{3+}. Typically, non-radiative energy transfer is responsible for concentration quenching, which can occur because of exchange interactions, light re-absorption, or multipole–multipole interactions. The exact nature of these interactions can be examined using Blasse's equation.[31]

$$R_C \approx 2\left[\frac{3V}{4\pi CN}\right]^{1/3} \quad (2)$$

Here, R_c denotes the critical separation distance between Eu^{3+}–Eu^{3+} ions, V represents the unit cell volume, C represents the optimal concentration of Eu^{3+} ions, and N signifies the number of Sr^{2+} ions in the unit cell.

Using V = 310 Å^3, C = 0.05 and N = 2 for the $Sr_3Ti_2O_7$ host, R_c was obtained as ~18 Å. This R_c value (>5 Å) suggested that the concentration quenching phenomenon is exclusively attributed to the multipole–multipole interaction.

Time-resolved decay measurements were conducted with an excitation wavelength of 395 nm, targeting the electric dipole transition $^5D_0 \rightarrow {}^7F_2$ of Eu^{3+}. Fig. 3(b) shows the decay curves at

Table 2 Judd–Ofelt parameters for Eu^{3+} doped $Sr_3Ti_2O_7$

Concentration (mol%)	Ω_2 (pm^2)	Ω_4 (pm^2)	Transitions	$A_{0-2,4}$ (s^{-1})	A_{0-1} (s^{-1})	A_T (s^{-1})	τ (ms)	β (%)	Asy. Ratio (R_{asy})
1	0.784	0.017	$^5D_0 \rightarrow {}^7F_1$		50	146.87	6.80	34.04	1.85
			$^5D_0 \rightarrow {}^7F_2$	95.81				65.23	
			$^5D_0 \rightarrow {}^7F_4$	1.06				0.72	
2	0.760	0.019	$^5D_0 \rightarrow {}^7F_1$		50	144.16	6.93	34.68	1.79
			$^5D_0 \rightarrow {}^7F_2$	92.97				64.49	
			$^5D_0 \rightarrow {}^7F_4$	1.19				0.82	
3	0.757	0.017	$^5D_0 \rightarrow {}^7F_1$		50	145.31	6.88	34.40	1.81
			$^5D_0 \rightarrow {}^7F_2$	94.27				64.87	
			$^5D_0 \rightarrow {}^7F_4$	1.04				0.66	
5	0.741	0.016	$^5D_0 \rightarrow {}^7F_1$		50	141.64	7.59	35.30	1.74
			$^5D_0 \rightarrow {}^7F_2$	90.65				64.00	
			$^5D_0 \rightarrow {}^7F_4$	0.99				0.67	
7	0.730	0.015	$^5D_0 \rightarrow {}^7F_1$		50	140.15	7.13	35.67	1.72
			$^5D_0 \rightarrow {}^7F_2$	89.20				63.65	
			$^5D_0 \rightarrow {}^7F_4$	0.95				0.67	

three different concentrations of Eu^{3+} (3 mol%, 5 mol% and 7 mol%) doped $Sr_3Ti_2O_7$ phosphors. All the decay transients were effectively matched using a bi-exponential formula, as represented by eqn (3):

$$I(t) = A_1 \exp\left(-\frac{t}{\tau_1}\right) + A_2 \exp\left(-\frac{t}{\tau_2}\right) \quad (3)$$

$I(t)$ represents the intensities at time t, and A_1 and A_2 are the weighting constant parameters. τ_1 and τ_2 correspond to the associated lifetimes. The mean decay time can be delineated using these factors as per ref. 32 and 33:

$$\tau_{avg} = \frac{A_1\tau_1^2 + A_2\tau_2^2}{A_1\tau_1 + A_2\tau_2} \quad (4)$$

The presence of a bi-exponential decay can be attributed to two main possible explanations. Firstly, it could be due to a difference in the non-radiative probability of decay for rare-earth ions at or near the surface and rare-earth ions in the core of the particles. Another is the inhomogeneous distribution of the rare-earth ions in the host material, leading to the variation in the local concentration.[32] The decay times for 3 mol%, 5 mol% and 7 mol% Eu^{3+} doped $Sr_3Ti_2O_7$ were determined as 0.50 ms, 0.37 ms and 0.27 ms, respectively. Introducing Eu^{3+} ions into $Sr_3Ti_2O_7$ during the doping process creates certain defects that function as trapping centers for charge carriers. Consequently, the obtained decay time results suggest that the depth of these traps is relatively shallow, facilitating a rapid escape of charge carriers from the traps. This quick escape leads to a fast recombination rate within the millisecond range (ms).

Judd–Ofelt analysis. The radiative transition within the $4f^6$ configuration of a Eu^{3+} ion can be analyzed in the framework of the Judd–Ofelt approach. The J–O intensity parameters Ω_j (j = 2, 4, 6) give valuable information concerning the symmetry and bonding of the rare earth ion within the host. Specifically, Ω_2 determines the polarization and asymmetric behavior of the rare-earth ion, representing a short-range effect. On the other hand, parameters such as Ω_4 and Ω_6 are associated with bulk properties like viscosity and rigidity, constituting long-range effects. Typically, these parameters are derived from absorption spectra. However, in our case, obtaining the absorption spectra of the powder sample is challenging. Nevertheless, we employed a determination methodology described by Kodaira *et al.*,[34] involving the utilization of the photoluminescence emission spectra originating from the specific energy level of Eu^{3+} ions to calculate the intensity parameters. This approach links the cumulative emission intensities arising from spontaneous radiative emission in the transition between the two manifolds $^5D_0 \rightarrow {}^7F_j$ (where j = 2, 4, 6) with the radiative emission rate.[35] It is important to note that the value of $A_{0\rightarrow6}$, and thus Ω_6, cannot be calculated since the $^5D_0 \rightarrow {}^7F_6$ transition was not observed in the emission spectra.

The expression for the radiative emission rate is stated as follows:

$$\frac{A_{0\rightarrow2,4}}{A_{0\rightarrow1}} = \left[\frac{I_{0\rightarrow2,4}}{I_{0\rightarrow1}}\frac{h\upsilon_{0\rightarrow1}}{h\upsilon_{0\rightarrow2,4}}\right] \quad (5)$$

In this context, $I_{0\rightarrow j}$ denotes the integrated emission intensity, and $h\upsilon_{0\rightarrow j}$ represents the energy associated with the $^5D_0 \rightarrow {}^7F_j$ (j = 1, 2, 4). In the scenario of a magnetic dipole transition, its characteristics remain unaltered by the crystal field. Therefore, the magnetic dipole radiative transition rate, denoted $A_{0\rightarrow1}$, is regarded as the s constant at 50 s^{-1}.

The spontaneous emission rate as a function of J–O parameters can be expressed as:

$$A_{O\rightarrow J} = \frac{64\pi^4\left(\upsilon_{0\rightarrow2,4}\right)^3}{3hC^3} e^2 \frac{1}{4\pi\varepsilon_0}\chi \sum_{J=2,4,6} \Omega_J < {}^5D_0 \left| U^{(J)} \right| {}^7F_{2,4} >^2 \quad (6)$$

Here, e denotes the elementary charge, and $\chi = n(n^2 + 2)^2/9$ represents the Lorentz local field correction factor, which is dependent on the host's refractive index n (with a value of 2.25). The square reduced matrix elements that are not equal to zero are $\langle {}^5D_0|U^{(2)}|{}^7F_2\rangle^2$, which is 0.0032, and $\langle {}^5D_0|U^{(4)}|{}^7F_4\rangle^2$, which is 0.0023, and it typically does not depend on the host.[35,36] Consequently, the Judd–Ofelt parameters for experimental intensity can be computed by analyzing the intensity ratio related to the transition $^5D_0 \rightarrow {}^7F_{2,4}$.

By utilizing the equation below, the total radiative transition probability, denoted as A_T, can be computed:

$$A_T(\psi J) = \sum_{J'} A_{J-J'} \quad (7)$$

Furthermore, the radiative lifetime of an excited state in terms of A_T, is given by:

$$\tau_{rad}(\psi J) = \frac{1}{A_T(\psi J)} \quad (8)$$

The branching ratio, denoted as $\beta(\psi J)$, assesses the proportion of emission attributed to a particular transition from a state in comparison to all other transitions originating from that state. It can be calculated using the following expression:

$$\beta(\psi J) = \frac{A(\psi J, \psi' J')}{A_T(\psi J)} \quad (9)$$

The J–O analysis reveals a consistent trend across all compositions of $Sr_{3(1-x)}Ti_2O_7$:xEu^{3+}, indicating that $\Omega_2 > \Omega_4$. This trend demonstrates the covalence between Eu^{3+} and O^{2-} and the notable asymmetry present at the Eu^{3+} site. A higher value of $\beta(\psi J)$ suggests that the $^5D_0 \rightarrow {}^7F_2$ transition (electrical dipole) shows increased sensitivity. This validates the enhanced and intense red emission observed in this layered perovskite material. For a comprehensive overview, the J–O parameters are summarized in Table 2.

Temperature-dependent photoluminescence studies and quantum yields. The effect of the elevated temperature on the PL properties of layered $Sr_{3(1-x)}Ti_2O_7$:xEu^{3+} phosphors particles are systematically investigated. The temperature stability of the optical properties is of great significance in evaluating luminescent materials, especially considering the potential exposure to high temperatures during long-term operation.

Fig. 4 illustrates the temperature-dependent PL emission of $Sr_3Ti_2O_7$ phosphors doped with 5 mol% Eu^{3+}. The measurements were performed using a 395 nm UV excitation over a wide temperature range of 300–450 K. It is widely recognized that thermal quenching mechanisms vary across different luminescent materials. The rapid decline in PL emission intensity with increasing temperature can be attributed to non-radiative processes. As the temperature rises, these non-radiative pathways become more dominant, reducing the luminescent output.

The probability of non-radiative transitions is directly proportional to the absolute temperature. Consequently, higher temperatures lead to an increased probability of non-radiative transitions, resulting in a decrease in PL emission intensity. Notably, the emission intensity of $Sr_3Ti_2O_7$ doped with 5 mol% Eu^{3+} exhibits remarkable retention, maintaining 75% of its initial value at 420 K compared to that at 300 K, as shown in Fig. 5(a). At room temperature, the radiative transition from the excited state $^5D_0$ to the ground state $^7F_0$ remains independent of temperature. However, as the temperature rises, the excited electrons acquire sufficient thermal energy to reach the crossover point between the $^5D_0$ excited state and the CTB, and subsequently relax to another crossover point between the $^7F_0$ state and the CTB. From this point, they undergo non-radiative transitions to reach the ground state.[37] The occurrence of non-radiative transitions increases at the crossover point, which represents the intersection between the ground state and the excited state of the Eu^{3+} ion.

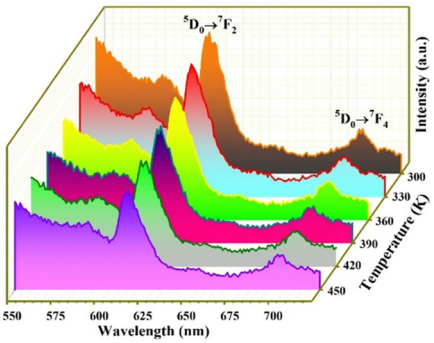

Fig. 4 Temperature-dependent PL emission spectra of 5 mol% doped $Sr_3Ti_2O_7$ phosphor upon 395 nm UV excitation source.

To comprehend the thermal quenching behavior of the layered $Sr_{3(1-x)}Ti_2O_7$:xEu^{3+} materials, the activation energy serves as an important parameter. It can be estimated using the Arrhenius equation,[25,37] which is expressed as follows:

$$I_T = \frac{I_0}{1 + A\exp(-\Delta E_a/kT)} \quad (10)$$

Emission intensity at different temperatures (T) is denoted by I_T, I_0 represents the intensity at the starting temperature, A denotes the frequency factor, ΔE_a represents the activation energy, and k is the Boltzmann constant. By plotting $\ln[I_0/I_T - 1]$ against $1/T$, as shown in Fig. 5(b), the slope of the graph is equal to $(-\Delta E_a/k)$, allowing the calculation of the activation energy. In this instance, the determined activation energy was identified to be 0.10 eV. The thermally activated nonradiative transition rate is inversely proportional to the activation energy (ΔE_a). Therefore, with an activation energy of 0.10 eV, it serves as a potential barrier for the electrons, preventing the occurrence of thermal quenching phenomena.

Furthermore, the absolute quantum yield is a significant characteristic reflecting light-emitting materials' performance and suitability for solid-state lighting applications. The quantum yield (η) quantifies the proportion of emitted photons (N_{emi}) relative to the absorbed photons (N_{abs}) in a specimen.[38,39] The subsequent equation has been employed for computing the value of 'η':

$$\eta = \frac{N_{emi}}{N_{abs}} = \frac{\int I_{emission}}{\int I_{reference} - \int I_{excitation}} \quad (11)$$

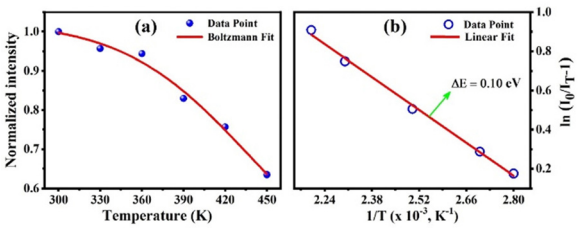

Fig. 5 (a) Variation of emission intensity as a function of temperature within 300–450 K for 5 mol% doped $Sr_3Ti_2O_7$ phosphor and (b) the Arrhenius plot for calculating activation energy.

In this equation, $I_{emission}$ represents the integral of the emission curve for the sample, $I_{reference}$ is the integral of the emission curve obtained by scanning over the excitation peak in the absence of the fluorescence sample, and $I_{excitation}$ corresponds to the integral of the excitation peak in the presence of the sample. The evaluations were conducted utilizing an integrating sphere to measure the sample. The quantum yield was calculated for optimized 5 mol% Eu^{3+} doped $Sr_3Ti_2O_7$ phosphor using a 395 nm UV light source. The quantum yields of various other Eu^{3+} doped phosphors are presented in Table 3.[40–49]

The phosphor demonstrates a notable quantum efficiency of 18%. In comparison, the widely known-Eu^{3+} doped Y_2O_3 and YVO_4 phosphors have a higher quantum yield.[48,49] For rare earth-doped YVO_4, a special benefit of host sensitization is obtained, as evidenced by our previous works.[50–52] Based on the provided data, it can be inferred that the $Sr_3Ti_2O_7$:5 mol% Eu^{3+} phosphor exhibits characteristics conducive to solid-state lighting applications.

Photometric characterization. Color coordinates were determined using the Commission Internationale de l'Eclairage (CIE) 1931 calculator program to assess the performance of the phosphors. Fig. 6 presents the CIE chromaticity coordinates of layered $Sr_{3(1-x)}Ti_2O_7$:xEu^{3+} when excited with 395 nm light. The color of any light source is determined by three tristimulus variables, denoted as variables $\bar{x}(\lambda)$, $\bar{y}(\lambda)$ and $\bar{z}(\lambda)$, which are referred to as color-matching functions. These functions play a crucial role in determining the color of a light source. The CIE tristimulus values are computed by mathematically integrating the spectral data, providing a means to determine the color coordinates.

The tristimulus values X, Y, and Z are expressed by the following equations:

$$X = \int \bar{x}(\lambda) P(\lambda) \mathrm{d}\lambda$$
$$Y = \int \bar{y}(\lambda) P(\lambda) \mathrm{d}\lambda \quad (12)$$
$$Z = \int \bar{z}(\lambda) P(\lambda) \mathrm{d}\lambda$$

Table 3 Quantum yields of Eu^{3+} doped phosphor materials

Materials	Excitation wavelength (nm)	Emission wavelength (nm)	Quantum yield (%)	Ref.
$BaZrO_3$:Eu^{3+}	279	625	14	40
0.8ZnO–0.2SrO–Al_2O_3:Eu^{3+}	393	620	12	41
ZrO_2:Eu^{3+}	395	606 and 615	4.8	42
$AlPO_4$:Eu^{3+}	392	594	22	43
$SrVO_3$:Eu^{3+}	420	500	14.36	44
$CaMoO_4$:Eu^{3+}	395	616	12.78	45
Dy^{3+} doped $Ca_2ZnSi_2O_7$:Eu^{3+}	394	615	12.88	46
$GdBO_3$:Eu^{3+}	391	591	14.3	47
YVO_4:Eu^{3+}	310	619	55.5	48
Y_2O_3:Eu^{3+}	395	623	23	49
$Sr_3Ti_2O_7$:Eu^{3+}	395	616	18	This work

The CIE color co-ordinate can be calculated by using the tristimulus values through the following relationships[53]

$$x = \frac{X}{X+Y+Z}$$
$$y = \frac{Y}{X+Y+Z} \quad (13)$$
$$z = \frac{Z}{X+Y+Z}$$

The CIE image shown in Fig. S2(a) (ESI†) indicates that the CIE color coordinates for layered $Sr_{3(1-x)}Ti_2O_7$:xEu^{3+} shift towards the pure red region as the doping concentration of Eu^{3+} increases. This shift is observed from the coordinates (0.62, 0.34) to (0.64, 0.31), corresponding to the characteristic emission region of Eu^{3+} ions.

However, when subjected to elevated temperatures, as shown in Fig. S2(b) (ESI†), the optimized composition of 5 mol% Eu^{3+} doped $Sr_3Ti_2O_7$ exhibits consistent color coordinates. At 300 K, the coordinates are (0.57, 0.38), and at 450 K, they remain the same (0.57, 0.38). This indicates that the prepared phosphor demonstrates remarkable thermal stability even at elevated temperatures. To assess the quality of the emitted light, it is important to estimate the correlated color CCT values of the prepared samples. The CCT values are determined using the McCamy empirical relationship,[54,55] given by:

$$\mathrm{CCT} = -437n^3 + 3601n^2 - 6861n + 5514.31 \quad (14)$$

where, $n = (x - x_e)/(y - y_e)$ and (x_e = 0.3320, y_e = 0.1858).

(x_e, y_e) represents the epicenters of the convergence. By calculating the CCT values using the CIE chromaticity coordinates obtained from the PL emission spectra, it was found that the values range from 2412 to 3452 K for the layered $Sr_{3(1-x)}Ti_2O_7$:xEu^{3+}. The optimized composition of 5 mol% Eu^{3+} doped $Sr_3Ti_2O_7$ exhibits a CCT value of 3452 K.

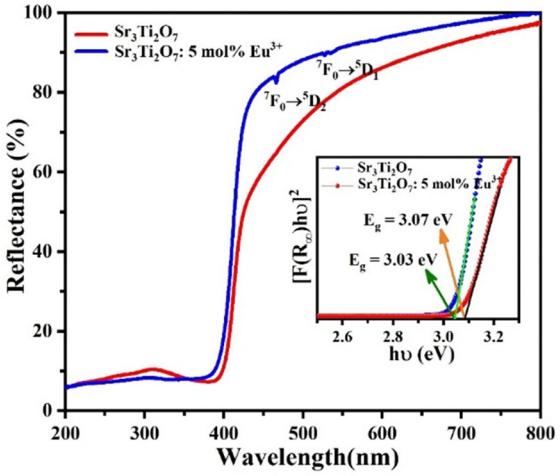

Fig. 6 Absorption spectra in the UV-visible range, obtained through diffuse reflectance mode of undoped $Sr_3Ti_2O_7$ and 5 mol% Eu^{3+} doped $Sr_3Ti_2O_7$ phosphors. The inset in the figure displays Kubelka–Munk plots used for determining the optical band gap energy of the two samples.

Typically, warm light used in home appliances has CCT values below 5000 K, while CCT values above 5000 K are suitable for cold light.[56] Therefore, the prepared phosphors can be considered as candidates for warm light emission.

Furthermore, the purity of the red color emitted from the layered $Sr_{3(1-x)}Ti_2O_7$:xEu^{3+} was evaluated using the following relationship:[16]

$$\text{Color purity} = \sqrt{\frac{(x_s - x_i)^2 + (y_s - y_i)^2}{(x_d - x_i)^2 + (y_d - y_i)^2}} \times 100 \quad (15)$$

where (x_s,y_s) and (x_i,y_i) represent the color co-ordinate of the sample point and the illuminant point, respectively, and (x_d,y_d) is the coordinate of dominant wavelength at 616 nm. The layered $Sr_{3(1-x)}Ti_2O_7$:xEu^{3+} exhibited good color purity, with the optimized composition showing a color purity of 89.18%. The photometric properties are summarized in Table 4.

UV-Visible absorption analysis and band gap of the material. Fig. 6 displays the diffuse reflectance (DR) spectra of $Sr_{3(1-x)}Ti_2O_7$:xEu^{3+}, recorded within 200–800 nm against the reference standard spectral on fluoropolymer. A prominent band ranging from 200 to 400 nm is observed in the DR spectra, corresponding to the band gap of $Sr_3Ti_2O_7$. Additionally, there are weaker transitions centered at 464 nm ($^7F_0 \rightarrow {}^5D_2$) and 530 nm ($^7F_0 \rightarrow {}^5D_1$) due to the presence of metastable energy states of Eu^{3+} formed between the valence and conduction band of the host material.

The electronic properties can be understood by investigating their band gap, which is a crucial parameter for optoelectronic device applications. To determine the optical band gap for layered $Sr_{3(1-x)}Ti_2O_7$:xEu^{3+}, the Kubelka–Munk method[57,58] is employed using the DR spectra. The Kubelka–Munk function $[F(R_\alpha)]$ can be expressed in terms of R_α as:

$$F(R_\alpha) = \frac{(1 - R_\alpha)^2}{2R_\alpha} = \frac{K}{S} \quad (16)$$

Here, R_α represents the ratio of the sample's reflectance (R_{sample}) to the reference's reflectance ($R_{reference}$), and K and S denote the absorption and scattering coefficients, respectively. The Tauc equation[58] establishes a connection between the absorption coefficient (α) and the incident photon energy ($h\upsilon$) for determining the optical bandgap. It is expressed as:

$$\alpha h\upsilon = C(h\upsilon - E_g)^{n/2} \quad (17)$$

In this context, υ denotes the frequency of the incident photon, E_g represents the ascertained optical band gap of the samples, C is a constant independent of energy, and assuming a direct allowed transition, n is considered to be 1. In the case of perfect diffuse scattering, it is assumed that, $K = 2\alpha$ and S remains constant throughout the wavelength of measurement.

To make the Tauc equation compatible with the Kubelka–Munk function and the associated absorption parameters, it can be modified as follows[58,59]:

$$F(R_\infty)h\upsilon = C(h\upsilon - E_g)^{n/2} \quad (18)$$

The inset of Fig. 6 illustrates the plot of $[F(R_\alpha)h\upsilon]^2$ *vs.* $h\upsilon$, where the Kubelka–Munk function and frequency are squared.

Table 4 CIE chromaticity color coordinate, CCT and color-purity for perovskite $Sr_3Ti_2O_7$:xEu^{3+}

	Color coordinate			
Concentration/Temperature	*X*	*Y*	CCT (K)	Color purity (%)
1 mol%	0.62	0.34	2412	84.02
2 mol%	0.64	0.34	2693	89.41
3 mol%	0.64	0.33	3027	89.25
5 mol%	0.64	0.32	3452	89.18
7 mol%	0.64	0.31	3027	89.25
300 K	0.57	0.38	1710	72.34
330 K	0.57	0.38	1710	72.34
360 K	0.56	0.38	1715	69.72
390 K	0.56	0.37	1710	69.10
420 K	0.57	0.38	1717	73.03
450 K	0.57	0.38	1710	69.10

By extrapolating the linear region of the plot to $[F(R_\alpha)h\upsilon]^2 = 0$, the optical band gap can be estimated. For both $Sr_3Ti_2O_7$ and 5 mol% Eu^{3+} doped $Sr_3Ti_2O_7$ materials, the obtained band gaps were found to be 3.03 eV and 3.07 eV, respectively, demonstrating their close proximity to each other.

Conclusions

The experimental results obtained in this study reveal that layered perovskite $Sr_{3(1-x)}Ti_2O_7$:xEu^{3+} has a tetragonal crystal structure with space group I4/mmm. When excited with 395 nm light, $Sr_{3(1-x)}Ti_2O_7$:xEu^{3+} exhibits strong photoluminescence behavior attributed to the transitions $^5D_0 \rightarrow {}^7F_j$ (j = 0–6) in the Eu^{3+} ion. Notably, when Eu^{3+} ions occupy the non-centrosymmetric sites, they emit intense and sharp light at 616 nm, corresponding to the hypersensitive transitions $^5D_0 \rightarrow {}^7F_2$. The observed value of R_c (~18 Å) confirms the concentration quenching phenomenon, indicating that multipole interactions play a role in the reduction of luminescence intensity with increasing dopant concentration. The optimized 5 mol% Eu^{3+} doped $Sr_3Ti_2O_7$ sample's quantum yield was 18%, indicating its suitability for efficient light emission.

The material also demonstrates favorable thermal stability, retaining 75% of the emission intensity at 420 K. The activation energy, determined to be 0.10 eV, indicates the energy barrier that prevents thermal quenching phenomena. Furthermore, the Judd–Ofelt analysis reveals a trend where $\Omega_2 > \Omega_4$ for all compositions of $Sr_{3(1-x)}Ti_2O_7$:xEu^{3+}, indicating covalence between Eu^{3+} and O^{2-} ions as well as a high degree of asymmetry at the Eu^{3+} sites. Additionally, the materials exhibit a millisecond-level lifetime for the $^5D_0$ state, stable CIE chromaticity coordinates, high color purity, and a CCT value suitable for lighting applications. These characteristics collectively suggest that the prepared layered perovskite $Sr_{3(1-x)}Ti_2O_7$:xEu^{3+} has great potential as a candidate for various lighting applications.

Author contributions

Dhananjay Kumar Singh: Conceptualization, Formal analysis, Investigation, Methodology, Writing – original draft. Shriya Sinha: Methodology, Formal analysis, Writing – review &

editing. Manoj Kumar Mahata: Formal analysis, Supervision, Writing – review & editing.

Conflicts of interest

The authors declare no conflicts of interest regarding this article.

Acknowledgements

M. K. M. gratefully acknowledges the support from the Alexander von Humboldt (AvH) Foundation, Germany.

Notes and references

1 M. A. Triana, E. L. Hsiang, C. Zhang, Y. Dong and S. T. Wu, Luminescent Nanomaterials for Energy-Efficient Display and Healthcare, *ACS Energy Lett.*, 2022, **7**, 1001–1020.
2 J. Meyer and F. Tappe, Photoluminescent Materials for Solid-State Lighting: State of the Art and Future Challenges, *Adv. Opt. Mater.*, 2015, **3**, 424–430.
3 S. Sinha, M. K. Mahata and K. Kumar, Up/down-converted green luminescence of Er^{3+}–Yb^{3+} doped paramagnetic gadolinium molybdate: a highly sensitive thermographic phosphor for multifunctional applications, *RSC Adv.*, 2016, **6**, 89642–89654.
4 L. Chen, C. C. Lin, C. W. Yeh and R. S. Liu, Light Converting Inorganic Phosphors for White Light-Emitting Diodes, *Materials*, 2010, **3**, 2172–2195.
5 R. Zhang, H. Lin, Y. yu, D. Chen, J. Xu and Y. Wang, A new-generation color converter for high-power white LED: transparent Ce^{3+}: YAG phosphor-in-glass, *Laser Photonics Rev.*, 2014, **8**, 158–164.
6 X. He, X. Liu, R. Li, B. yang, K. Yu, M. Zeng and R. Yu, Effects of local structure of Ce^{3+} ions on luminescent properties of $Y_3Al_5O_{12}$: Ce nanoparticles, *Sci. Rep.*, 2016, **6**, 22238.
7 S. K. Gupta, R. M. Kadam and P. K. Pujari, Lanthanide spectroscopy in probing structure-property correlation in multi-site photoluminescent phosphors, *Coord. Chem. Rev.*, 2020, **420**, 213405.
8 D. K. Singh, K. Mondal and J. Manam, Improved photoluminescence, thermal stability and temperature sensing performances of K^+ incorporated perovskite $BaTiO_3$:Eu^{3+} red emitting phosphors, *Ceram. Int.*, 2017, **43**, 13602–13611.
9 X. Gong, H. Jiang, M. Cao, Z. Rao, X. Zhao and A. Vomiero, Eu-doped ZnO quantum dots with solid-state fluorescence and dual emission for high-performance luminescent solar concentrators, *Mater. Chem. Front.*, 2021, **5**, 4746–4755; P. Du, W. Ran, Y. Hou, L. Luo and W. Li, Eu^{3+}-Activated $NaGdF_4$ Nanorods for Near-Ultraviolet Light-Triggered Indoor Illumination, *ACS Appl. Nano Mater.*, 2019, **2**(7), 4275–4285.
10 N. Katumo, G. Gao, F. Laufer, B. S. Richards and I. A. Howard, Smartphone-based luminescent thermometry via temperature-sensitive delayed fluorescence from Gd_2O_2S: Eu^{3+}, *Adv. Opt. Mater.*, 2020, **8**, 2000507; R. Chatterjee, S. Saha, D. Sen, K. Panigrahi, U. K. Ghorai, G. C. Das and K. K. Chattopadhyay, Neutralizing the Charge Imbalance Problem in Eu^{3+}-Activated $BaAl_2O_4$ Nanophosphors: Theoretical Insights and Experimental Validation Considering K^+ Co-doping, *ACS Omega*, 2018, **3**, 788–800.
11 D. K. Singh and J. Manam, Investigation of structural, spectral and photometric properties of $CaTiO_3$:Dy^{3+} nanophosphors for the lighting applications, *Electron. Mater. Lett.*, 2017, **13**, 292–301.
12 M. K. Mahata, K. Kumar and V. K. Rai, Structural and optical properties of Er^{3+}/Yb^{3+} doped barium titanate phosphor prepared by co-precipitation method, *Spectrochim. Acta, Part A*, 2014, **124**, 285–291.
13 P. P. Sukul, M. K. Mahata, U. K. Ghorai and K. Kumar, Crystal phase induced upconversion enhancement in Er^{3+}/Yb^{3+} doped SrTiO3 ceramic and its temperature sensing studies, *Spectrochim. Acta, Part A*, 2019, **212**, 78–87.
14 M. K. Mahata, T. Koppe, K. Kumar, H. Hofsäss and U. Vetter, Upconversion photoluminescence of Ho^{3+}–Yb^{3+} doped barium titanate nanocrystallites: Optical tools for structural phase detection and temperature probing, *Sci. Rep.*, 2020, **10**, 8775.
15 S. P. Tiwari, M. K. Mahata, K. Kumar and V. K. Rai, Enhanced temperature sensing response of upconversion luminescence in ZnO–$CaTiO_3$: Er^{3+}/Yb^{3+} nano-composite phosphor, *Spectrochim. Acta, Part A*, 2015, **150**, 623–630.
16 D. K. Singh and J. Manam, Optical spectroscopic and thermal quenching behaviour of perovskite $SrTiO_3$:Sm^{3+} orange emitting phosphors for lighting applications, *J. Mater. Sci.: Mater. Electron.*, 2018, **29**, 5588.
17 L. Zhang, B. Sun, Q. Liu, N. Ding, H. Yang, L. Wang and Q. Zhang, Novel layered perovskite $Sr_3Ti_2O_7$:Eu^{3+} phosphor with high-efficiency luminescence enhanced by charge compensation, *J. Alloys Compd.*, 2016, **657**, 27–31.
18 V. Jeyalakshmi, R. Mahalakshmy, K. Ramesh, P. V. C. Rao, N. V. Choudary, G. S. Ganesh, K. Thirunavukkarasu, K. R. Krishnamurthy and B. Viswanathan, Visible light driven reduction of carbon dioxide with water on modified $Sr_3Ti_2O_7$ catalysts, *RSC Adv.*, 2015, **5**, 5958.
19 S. Kamba, P. Samoukhina, F. Kadlec, J. Pokorný, J. Petzelt, I. M. Reaney and P. L. Wise, Composition dependence of the lattice vibrations in $Sr_{n+1}TinO_{3n+1}$ Ruddlesden–Popper homologous series, *J. Eur. Ceram. Soc.*, 2003, **23**(14), 2639–2645.
20 Y. Inaguma, D. Nagasawa and T. Katsumata, Photoluminescence of Praseodymium-Doped Srn+1TinO3n+1 (n = 1, 2, ∞), *Jpn. J. Appl. Phys.*, 2005, **44**, 761.
21 L. Zhang, B. Sun, Q. Liu, N. Ding, H. Yang, L. Wang and Q. Zhang, Novel layered perovskite $Sr_3Ti_2O_7$: Eu^{3+} phosphor with high-efficiency luminescence enhanced by charge compensation, *J. Alloys Compd.*, 2016, **657**, 27–31.
22 W. Ge, C. Zhu, H. An, Z. Li, G. Tang and D. Hou, Sol–gel synthesis and dielectric properties of Ruddlesden–Popper phase $Sr_{n+1}Ti_nO_{3n+1}$ (n = 1, 2, 3, ∞), *Ceram. Int.*, 2014, **40**, 1569–1574.

23 M. Tang, P. Fuierer, P. Dickens and E. Fu, Irradiation study on $Sr_{n+1}Ti_nO_{3n+1}$ Ruddlesden-Popper phases synthesized by hot-forging, *Phys. Status Solidi C*, 2013, **10**, 216–220.
24 R. Ganguly, V. Siruguri, I. K. Gopalakrishnan and J. V. Yakhmi, Stability of the layered $Sr_3Ti_2O_7$ structure in $La_{1.2}(Sr_{1-x}Ca_x)_{1.8}Mn_2O_7$, *J. Phys.: Condens. Matter*, 2000, **12**, 1683–1689.
25 D. K. Singh, K. Mondal and J. Manam, Efficient dual emission mode of green emitting perovskite $BaTiO_3$: Er^{3+} phosphors for display and temperature sensing applications, *Ceram. Int.*, 2017, **43**, 13602–13611.
26 S. Sinha, M. K. Mahata and K. Kumar, Enhancing the upconversion luminescence properties of Er^{3+}–Yb^{3+} doped yttrium molybdate through Mg^{2+} incorporation: effect of laser excitation power on temperature sensing and heat generation, *New J. Chem.*, 2019, **43**, 5960–5971.
27 Q. Lv, X. ma, Y. Dong, Y. Li, B. Shao, C. Wang, S. Yang and C. Wang, Blue light-excitable Eu-doped yellow emitting borate $KSr_4B_3O_9$ phosphor for white light-emitting diodes, *J. Am. Ceram.*, 2022, **105**, 7374–7383.
28 M. Rajendran and S. Vaidyanathan, A Novel Highly Efficient Host-Sensitized Red Emitting ($Ba_2YV_3O_{11}$:Eu^{3+}) Phosphor for Hybrid White LEDs, *Chemistry Select*, 2020, **5**, 5128–5136.
29 J. Petry, R. Komban, C. Gimmler and H. Weller, Simple one pot synthesis of luminescent europium doped yttrium oxide Y2O_3: Eu nanodiscs for phosphor converted warm white LEDs, *Nanoscale Adv.*, 2022, **4**, 858–864.
30 R. Bajaj, A. S. Rao and G. V. Prakash, Linear and nonlinear photoluminescence from thermally stable KYF_4:Eu^{3+} cubic nanocrystals, *J. Alloys Compd.*, 2021, **885**, 160893.
31 G. Blasse, Energy transfer between inequivalent Eu2+ ions, *J. Solid State Chem.*, 1986, **62**, 207–211.
32 S. Dutta, S. Som and S. K. Sharma, Excitation spectra and luminescence decay analysis of K^+ compensated Dy^{3+} doped $CaMoO_4$ phosphors, *RSC Adv.*, 2015, **5**, 7380–7387.
33 S. Sinha and K. Kumar, Studies on up/down-conversion emission of Yb^{3+} sensitized Er^{3+} doped $MLa_2(MoO_4)_4$ (M = Ba, Sr and Ca) phosphors for thermometry and optical heating, *Opt. Mater.*, 2018, **75**, 770–780.
34 C. A. Kodaira, H. F. Brito and M. C. F. C. Felinto, Luminescence investigation of Eu^{3+} ion in the $RE_2(WO_4)_3$ matrix (RE = La and Gd) produced using the pechini method, *J. Solid State Chem.*, 2003, **171**, 401–407.
35 V. Mahalingam and J. Thirumalai, Facile hydrothermal synthesis and pulsed laser deposition of $Ca_{0.5}Y_{1-x}(WO_4)_2$:$x$$Eu^{3+}$ phosphors: investigations on the luminescence, Judd–Ofelt analysis and charge compensation mechanism, *New J. Chem.*, 2017, **41**, 493–502.
36 D. L. Shruthi, A. J. Reddy, G. N. A. Kumar and C. K. Jayasankar, Judd Ofelt theoretical analysis, Photoluminescence properties of Eu^{3+} activated $LiGd(WO_4)_2$ phosphors, *J. Lumin.*, 2020, **222**, 111167.
37 F. Chen, M. N. Akram and X. Chen, Improved Photoluminescence Performance of Eu^{3+}-Doped $Y_2(MoO_4)_3$ Red-Emitting Phosphor via Orderly Arrangement of the Crystal Lattice, *Molecules*, 2023, **28**, 1014.
38 B. P. Singh, A. K. Parchur, R. S. Ningthoujam, A. A. Ansari, P. Singh and S. B. Rai, *Dalton Trans.*, 2014, **43**, 4779–4789.
39 N. Verma, M. M. Domanska, T. Ram, J. Kaur, A. K. Misra, V. Dubey, N. Dubey, K. Tiwari and M. C. Rao, Optimizing the luminescence efficiency of an europium (Eu^{3+}) doped SrY_2O_4 phosphor for flexible display and lighting applications, *RSC Adv.*, 2023, **13**, 20217–20228.
40 S. K. Gupta, H. Abdou, C. U. Segre and Y. Mao, *Nanomaterials*, 2022, **12**, 3028.
41 Revupriya, P. S. Anjana, N. Gopakumar and M. S. Anju, *Mater. Res. Express*, 2020, **7**, 026203.
42 A. A. Nashivochnikov, A. I. Kostyukov, A. V. Zhuzhgov, M. I. Rakhmanova, S. V. Cherepanova and V. N. Snytnikov, *Opt. Mater.*, 2021, **121**, 111620.
43 Y. Liu, Z. Yang and Q. Yu, *J. Alloys Compd.*, 2011, **509**, L199–L202.
44 M. R. Patel, T. J. Park and S. K. Kailasa, *J. Photochem. Photobiol., A*, 2024, **449**, 115376.
45 F. B. Cao, L. S. Li, Y. W. Tian, Y. J. Chen and X. R. Wu, *Thin Solid Films*, 2011, **519**, 7971–7976.
46 K. Mondal and J. Manam, *J. Lumin.*, 2018, **195**, 259–270.
47 Z. Leng, N. Zhang, Y. Liu, L. Li and S. Gan, *Appl. Surf. Sci.*, 2015, **330**, 270.
48 L. Yang, G. Li, M. Zhao, J. Zheng, X. Guan and L. Li, Preparation and morphology-sensitive luminescence properties of Eu^{3+}-doped YVO_4: a defect chemistry viewpoint of study, *CrystEngComm*, 2012, **14**, 3227–3235.
49 D. Stefańska, M. Stefański and P. J. Dereń, Synthesis and spectroscopic characterization of the $K_4BaSi_3O_9$:Eu^{3+}, *Opt. Mater.*, 2014, **37**, 410–413.
50 M. K. Mahata, T. Koppe, K. Kumar, H. Hofsäss and U. Vetter, Demonstration of temperature dependent energy migration in dual-mode YVO_4: Ho^{3+}/Yb^{3+} nanocrystals for low temperature thermometry, *Sci. Rep.*, 2016, **6**, 36342.
51 M. K. Mahata, K. Kumar and V. K. Rai, Er^{3+}–Yb^{3+} doped vanadate nanocrystals: A highly sensitive thermographic phosphor and its optical nanoheater behaviour, *Sens. Actuators, B*, 2015, **209**, 775–780.
52 M. K. Mahata, S. P. Tiwari, S. Mukherjee, K. Kumar and V. K. Rai, YVO_4: Er^{3+}/Yb^{3+} phosphor as multifunctional applications, *J. Opt. Soc. Am. B*, 2014, **31**, 1814–1821.
53 J. P. C. do Nascimento, F. F. do Carmo, M. X. Facanha, J. E. V. de Morais, A. J. M. Sales, H. D. de Andrade, I. S. Q. Junior and A. S. B. Sombra, Visible and near-infrared luminescent properties of Pr^{3+}/Yb^{3+} co-doped lanthanum ortho-niobate phosphors, *Opt. Mater.*, 2019, **97**, 109399.
54 C. S. McCamy, Correlated color temperature as an explicit function of chromaticity coordinates, *Color Res. Appl.*, 1992, **17**, 142–144.
55 M. K. Raju, R. K. Samudrala, P. Yadav and A. Azeem, Color-Tunable Eu^{3+}, Eu^{2+}-Activated $CaSiO_3$ Nano Phosphor Extract from Agricultural-Recycling-Food-Waste Materials for Display Applications, *Adv. Photonics Res.*, 2023, **4**, 2200266.
56 A. Ghosh, P. Selvaraj, S. Sundaram and T. K. Mallick, The colour rendering index and correlated colour temperature

of dye-sensitized solar cell for adaptive glazing application, *Sol. Energy*, 2018, **163**, 537–544.

57 P. Kubelka, New Contributions to the Optics of Intensely Light-Scattering Materials. Part I, *J. Opt. Soc. Am.*, 1948, **38**, 448–457.

58 A. E. Morales, E. S. Mora and U. Pal, Use of diffuse reflectance spectroscopy for optical characterization of un-supported nanostructures, *Rev. Mex. Fis. S*, 2007, **53**, 18–22.

59 M. K. Mahata, T. Koppe, T. Mondal, C. Brusewitz, K. Kumar, V. K. Rai, H. Hofsass and U. Vetter, Incorporation of Zn^{2+} ions into $BaTiO_3$:Er^{3+}/Yb^{3+} nanophosphor: an effective way to enhance upconversion, defect luminescence and temperature sensing, *Phys. Chem. Chem. Phys.*, 2015, **17**, 20741.